


 Cite this: *RSC Adv.*, 2019, **9**, 15900

## An amorphous $\text{MoS}_x$ modified $\text{g-C}_3\text{N}_4$ composite for efficient photocatalytic hydrogen evolution under visible light†

 Xia Li,<sup>a</sup> Bo Wang,<sup>a</sup> Xia Shu,<sup>a</sup> Dongmei Wang,<sup>a</sup> Guangqing Xu,<sup>a</sup> Xinyi Zhang,<sup>a</sup> Jun Lv<sup>a</sup>  <sup>\*a</sup> and Yucheng Wu<sup>a</sup>  <sup>\*ac</sup>

In this work, an  $\text{MoS}_x/\text{g-C}_3\text{N}_4$  composite photocatalyst was successfully fabricated by a sonochemical approach, where amorphous  $\text{MoS}_x$  was synthesized using a hydrothermal method with  $\text{Na}_2\text{MoO}_4 \cdot \text{H}_2\text{O}$ ,  $\text{H}_4\text{SiO}_4(\text{W}_3\text{O}_9)_4$  and  $\text{CH}_3\text{CSNH}_2$  as precursors, and  $\text{g-C}_3\text{N}_4$  nanosheets were produced using a two-step thermal polycondensation method. The hydrogen-evolution performance of the  $\text{MoS}_x/\text{g-C}_3\text{N}_4$  composite was tested under visible light. The results show that the  $\text{H}_2$ -evolution rate of the  $\text{MoS}_x/\text{g-C}_3\text{N}_4$  (7 wt%) photocatalyst reaches a maximum value of  $1586 \mu\text{mol g}^{-1} \text{h}^{-1}$ , which is about 70 times that of pure  $\text{g-C}_3\text{N}_4$  nanosheets. The main reason is that amorphous  $\text{MoS}_x$  forms intimate heterojunctions with  $\text{g-C}_3\text{N}_4$  nanosheets, and the introduction of  $\text{MoS}_x$  into  $\text{g-C}_3\text{N}_4$  nanosheets not only enhances the ability to convert  $\text{H}^+$  into  $\text{H}_2$ , but also promotes the separation of photoinduced electron–hole pairs for the photocatalyst. BET analysis shows that the specific surface area and pore volume of  $\text{g-C}_3\text{N}_4$  are decreased in the presence of  $\text{MoS}_x$ . XPS analysis manifests that  $\text{MoS}_x$  provides a number of active sites. Mott–Schottky plots show that the conduction band of  $\text{MoS}_x$  ( $-0.18 \text{ V}$  vs.  $E_{\text{Ag}/\text{AgCl}}$ ,  $\text{pH} = 7$ ) is more negative than that of  $\text{g-C}_3\text{N}_4$  nanosheets.

Received 29th November 2018  
 Accepted 17th April 2019

DOI: 10.1039/c8ra09806a  
[rsc.li/rsc-advances](http://rsc.li/rsc-advances)

## 1. Introduction

With the intensification of the energy crisis and environmental pollution, the human need for green and renewable energy has become more urgent. Recently, research into and applications of solar energy have attracted great attention.<sup>1,2</sup> There is little doubt that once solar energy is fully utilized, mankind can solve the energy crisis and alleviate environmental pollution. Hydrogen, a clean fuel with its combustion product being environmentally friendly water, is a suitable substitute for petroleum fuels.<sup>3</sup> Furthermore, hydrogen can be obtained by water splitting in large quantities, so how to utilize solar energy to produce hydrogen by water splitting has become one of the key issues in achieving sustainable development.<sup>4</sup> In recent years, the hydrogen evolution reaction (HER) by semiconductors has increasingly become the focus of research. Scientists have conducted extensive and in-depth studies on solar-driven water splitting to obtain hydrogen using

semiconductors such as  $\text{TiO}_2$ ,<sup>5</sup>  $\text{CdS}$ ,<sup>6,7</sup> and graphene.<sup>8</sup> However, these materials have many different drawbacks, including the narrow range of response to visible light, environmental hazards and poor stability, which severely restrict their practical applications. For these reasons, the development of novel visible light responsive photocatalysts with high efficiency and good stability has become an important research direction.

Graphitic carbon nitride ( $\text{g-C}_3\text{N}_4$ ), a non-metallic semiconductor with a two-dimensional structure like graphene, has received great attention in the field of photocatalysis, due to its earth-abundance, high physicochemical stability, suitable band structure ( $E_g = 2.7 \text{ eV}$ ) and low cost.<sup>9,10</sup> Since it was first reported as a metal-free semiconductor photocatalyst for  $\text{H}_2$  production in 2009,<sup>11</sup>  $\text{g-C}_3\text{N}_4$  has become a potential novel photocatalytic material for hydrogen production. Nevertheless, the photocatalytic performance of  $\text{g-C}_3\text{N}_4$  is typically limited due to its high recombination of photoexcited electron–hole pairs, small surface area and low quantum efficiency.<sup>12,13</sup> Different methods have been used to improve its photocatalytic properties by nanostructure modulation,<sup>14–16</sup> ion doping,<sup>17,18</sup> loading with co-catalysts,<sup>19</sup> as well as compounding with other semiconductors.<sup>20</sup>

Molybdenum sulfide is a layered transition-metal dichalcogenide, which has been considered a promising candidate to replace Pt as a co-catalyst for HER. Molybdenum sulfide has superior properties, such as low cost, relative abundance, tunable band structure and absorption of visible light.

<sup>a</sup>School of Material Sciences and Engineering, Hefei University of Technology, Hefei 230009, China. E-mail: [ycwu@hfut.edu.cn](mailto:ycwu@hfut.edu.cn); [lyjun17@126.com](mailto:lyjun17@126.com)

<sup>b</sup>Guangxi Key Laboratory for Electrochemical Energy Materials, Guangxi University, Nanning, 530004, China

<sup>c</sup>Anhui Provincial Key Laboratory of Advanced Functional Materials and Devices, Hefei University of Technology, Hefei 230009, China

† Electronic supplementary information (ESI) available. See DOI: [10.1039/c8ra09806a](https://doi.org/10.1039/c8ra09806a)



Crystalline  $\text{MoS}_2$  has been reported to be an excellent catalyst for both photocatalytic and electrocatalytic HER due to the existence of active sites derived from the sulfur edges of  $\text{MoS}_2$  crystal layers.<sup>21,22</sup> Reports have always focused on  $\text{MoS}_2$  as a co-catalyst to enhance the photocatalytic activity of HER under visible light: for example,  $\text{MoS}_2/\text{C}_3\text{N}_4$ ,<sup>23,24</sup>  $\text{MoS}_2/\text{CdS}$ ,<sup>25</sup>  $\text{MoS}_2/\text{graphene}$ <sup>26</sup> and  $\text{MoS}_2/\text{TiO}_2$ .<sup>27</sup> Crystalline  $\text{MoS}_2$  has two distinct phases: the 2H-phase and the 1T-phase. 2H- $\text{MoS}_2$  exists in the natural environment and is more stable than 1T- $\text{MoS}_2$ , but its poor electrical conductivity limits its performance for HER. Whereas 1T- $\text{MoS}_2$  has high electron transfer capability and has been a vital research object.<sup>28</sup> In addition, amorphous molybdenum sulfide ( $\text{MoS}_x$ ) has also been found to be highly active for HER because of its ample unsaturated atoms.<sup>29</sup> In fact, amorphous  $\text{MoS}_x$  has recently been demonstrated to be an excellent co-catalyst because of its active centers for HER. Huogen Yu and colleagues declared that an amorphous molybdenum sulfide modified  $\text{g-C}_3\text{N}_4$  composite exhibits an obviously higher hydrogen-evolution activity than that of a crystalline molybdenum sulfide modified  $\text{g-C}_3\text{N}_4$  composite.<sup>30</sup> More recently, Xiao Hai and colleagues further demonstrated that the co-catalytic performance of monolayer  $\text{MoS}_2$  could be gradually enhanced by reducing its crystallinity, and a poorly crystalline  $\text{MoS}_2$  monolayer shows even higher co-catalytic performance than that of Pt.<sup>31</sup>

Herein, a novel kind of  $\text{MoS}_x/\text{g-C}_3\text{N}_4$  composite has been prepared by a sonochemical approach. The  $\text{g-C}_3\text{N}_4$  nanosheets were synthesized by a thermal polycondensation method. The amorphous  $\text{MoS}_x$  was synthesized by a hydrothermal method. The photocatalytic HER of  $\text{MoS}_x/\text{g-C}_3\text{N}_4$  was investigated and the mechanism of  $\text{MoS}_x/\text{g-C}_3\text{N}_4$  in improving the photocatalytic activity is discussed in detail. This work supplies a novel strategy for using amorphous  $\text{MoS}_x$  as a co-catalyst to enhance the photocatalytic HER of  $\text{g-C}_3\text{N}_4$  under visible light.

## 2. Experimental

### 2.1 Preparation

**2.1.1 Preparation of an ultrathin  $\text{g-C}_3\text{N}_4$  nanosheet photocatalyst.** The  $\text{g-C}_3\text{N}_4$  nanosheets were prepared by a two-step thermal polycondensation method using melamine powder as the precursor.<sup>9,32</sup> In detail, 10 g of melamine was calcined in air at 550 °C for 4 h at a heating rate of 8 °C min<sup>-1</sup>, then cooled down to room temperature. The obtained bulk  $\text{g-C}_3\text{N}_4$  was milled into powder and then 0.4 g of the powder was heated at 500 °C for 2 h at a heating rate of 5 °C min<sup>-1</sup> to prepare the  $\text{g-C}_3\text{N}_4$  nanosheets. Finally, 50 mg of the  $\text{g-C}_3\text{N}_4$  nanosheets was dispersed in 80 mL of deionized water at room temperature and exfoliated by ultrasonication for 2 h. The final product was centrifuged at 12 000 rpm and dried at 60 °C for 12 h and was named UCN.

**2.1.2 Preparation of amorphous  $\text{MoS}_x$  and crystalline  $\text{MoS}_2$ .** The amorphous  $\text{MoS}_x$  was prepared by a hydrothermal method. 0.2419 g of  $\text{Na}_2\text{MoO}_4 \cdot \text{H}_2\text{O}$ , 2.878 g of  $\text{H}_4\text{SiO}_4(\text{W}_3\text{O}_9)_4$  (silicotungstic acid) and 0.4508 g of  $\text{CH}_3\text{CSNH}_2$  were dissolved in 45 mL of deionized water and stirred for 1 h. The solution was then transferred to a 50 mL Teflon-lined stainless-steel autoclave. The autoclave was sealed tightly and maintained at 240 °C

for 24 h. After naturally cooling down to room temperature, the obtained black solution was centrifuged at 10 000 rpm and the obtained precipitates were washed with deionized water and ethanol several times. The product was dried in a vacuum at 60 °C for 8 h and milled into powder, and denoted as primitive  $\text{MoS}_x$ . 50 mg of the primitive  $\text{MoS}_x$  was dispersed in 80 mL of deionized water at room temperature and exfoliated by ultrasonication for 2 h. The final product was centrifuged at 12 000 rpm, dried at 60 °C for 12 h and named  $\text{MoS}_x$ . Crystalline  $\text{MoS}_2$  was obtained by heating the primitive  $\text{MoS}_x$  at 360 °C in ambient  $\text{N}_2$  for 2 h.

**2.1.3 Fabrication of  $\text{MoS}_x/\text{UCN}$  and  $\text{MoS}_2/\text{UCN}$  composite photocatalyst.** The  $\text{MoS}_x/\text{UCN}$  photocatalyst was fabricated by a green environmental sonochemical approach. For the typical procedure, 3.5 mg of primitive  $\text{MoS}_x$  and 50 mg of  $\text{g-C}_3\text{N}_4$  nanosheets were dissolved in 80 mL of deionized water. The suspension was ultrasonicated for 2 h and then dried at 60 °C for 12 h. With this method, the amorphous  $\text{MoS}_x/\text{UCN}$  composite photocatalyst was synthesized, denoted as  $\text{MoS}_x/\text{UCN}$  (7 wt%). By changing the amount of added  $\text{MoS}_x$  (1.5–5.5 mg),  $\text{MoS}_x/\text{UCN}$  (3–11 wt%), composite photocatalysts with different mass ratios of  $\text{MoS}_x$  can be obtained.  $\text{MoS}_2/\text{UCN}$  (7 wt%) was prepared by heating  $\text{MoS}_x/\text{UCN}$  (7 wt%) in ambient  $\text{N}_2$  at 360 °C for 2 h.

### 2.2 Characterization

The power X-ray diffraction (XRD) patterns of the samples were recorded by a Rigaku D/MAX2500V X-ray diffractometer (Cu  $\text{K}\alpha$ 1 irradiation,  $\lambda = 0.15406 \text{ \AA}$ ). Transmission electron microscopy (TEM) was performed with an electron microscope (JEM-2100F, Japan) operating at 200 kV. The BET specific surface and pore volume of the samples were determined by a surface area and pore size analyzer (Quadrasorb evo, USA). X-ray photoelectron spectroscopy (XPS) analysis of the samples was performed using an ESCALAB250Xi photoelectron spectrometer (Thermo) with monochromatic Al  $\text{K}\alpha$  (1486.60 eV). The UV-vis spectra of the samples were measured on a UV-vis spectrophotometer (UV-3600, Shimadzu Corp, Japan). The photoluminescence (PL) spectra of the samples were measured using a fluorescence spectrophotometer (F-4500) with an excitation wavelength of 315 nm.

### 2.3 Photocatalytic hydrogen production

Photocatalytic  $\text{H}_2$  production experiments were performed in a 300 mL sealed quartz reactor at room temperature. A 300 W Xe lamp with a UV-cutoff filter ( $\lambda > 400 \text{ nm}$ ) was used as the light source. In a typical photocatalytic experiment, 20 mg of photocatalyst power and 10 mL of triethanolamine were added into the quartz reactor, which contained 90 mL of deionized water, and were sonicated for 1 min. Before the photocatalytic experiments, the quartz reactor was degassed and maintained under vacuum conditions for 30 min by a vacuum pump, to remove the dissolved oxygen and ensure anaerobic conditions. Then, the suspensions were stirred and irradiated for 5 h. The amount of  $\text{H}_2$  released was measured by gas chromatography (FULI-9790II, with high-purity argon as the carrier gas).



## 2.4 Photoelectrochemical measurements

The electrochemical tests were carried out on a CHI660C electrochemical analyzer (Chenhua Instrument, Inc.) in a standard three-electrode configuration with a Pt sheet (1 cm<sup>2</sup> surface area) used as the counter electrode, Ag/AgCl (in saturated KCl) as the reference electrode, fluorine-doped tin oxide (FTO, 2 cm<sup>2</sup> surface area) deposited with photocatalysts serving as a working electrode and 0.5 M Na<sub>2</sub>SO<sub>4</sub> aqueous solution as the electrolyte. The working electrode was prepared as follows: 5 mg of photocatalyst power was mixed with 0.5 mL of ethyl alcohol, then 0.3 mL of Nafion solution (5 wt%) was added into the mixture to make a slurry by ultrasonic dispersal for 10 min. The slurry was uniformly dropped onto the working electrode. After drying at room temperature, the working electrode was transferred to a laboratory tube furnace and kept at 100 °C for 30 min in ambient N<sub>2</sub>. The photocurrent measurements were performed under the visible light irradiation of a 300 W Xe lamp with a UV-cutoff filter ( $\lambda > 400$  nm) and a potential of -0.1 V vs. Ag/AgCl. The EIS experiments were conducted in the frequency range from 100 kHz to 0.01 Hz, with an amplitude voltage of 5 mV at the open circuit voltage. Mott-Schottky analysis was carried out with potentials ranging from -0.9 to 0.1 V vs. Ag/AgCl for UCN and -0.12 to 0.06 V vs. Ag/AgCl for MoS<sub>x</sub> with an amplitude voltage of 5 mV.

## 3. Results and discussion

### 3.1 Characterization

The MoS<sub>x</sub>/UCN composite was synthesized by a sonochemical method, as schematically illustrated in Fig. 1. The XRD patterns of primitive MoS<sub>x</sub> and MoS<sub>2</sub> are shown in Fig. 2(a). Amorphous MoS<sub>x</sub> has only one weak and broad distinct diffraction peak at 14.4°. This demonstrates that the MoS<sub>x</sub> synthesized in this study has a very low crystallinity/amorphous structure, which is different from other MoS<sub>2</sub> synthesized by a hydrothermal method.<sup>33,34</sup> This is probably because H<sub>4</sub>SiMo<sub>12</sub>O<sub>40</sub> is involved in the reaction.<sup>35</sup> After calcination, amorphous MoS<sub>x</sub> can transform into crystallized MoS<sub>2</sub>. The XRD pattern of MoS<sub>2</sub> has three distinct diffraction peaks at 14.4°, 32.9° and 58.2° corresponding to the (002), (100) and (110) planes of 2H-MoS<sub>2</sub> (JCPDS no. 87-1526, molybdenum disulfide 2H), respectively. Fig. 2(b) shows XRD patterns of g-C<sub>3</sub>N<sub>4</sub> nanosheets and ultrathin g-C<sub>3</sub>N<sub>4</sub> with different contents of MoS<sub>x</sub>. For all samples, two diffraction peaks occur at 13.1° and 27.8°, and are indexed to be the (100) and (002) planes of g-C<sub>3</sub>N<sub>4</sub> (JCPDS 87-1526). The strongest peak of (002) at about 27.8° is attributed to the inter-planar stacking

of aromatic systems. The weak peak of (100) at 13.1° is induced by the in-plane structural stacking motif. The slight decrease in diffraction peak in the MoS<sub>x</sub>/UCN samples indicates that ultrathin g-C<sub>3</sub>N<sub>4</sub> with less stacking is produced due to the exfoliation of g-C<sub>3</sub>N<sub>4</sub> nanosheets in ultrasonic processing. Nevertheless, diffraction peaks corresponding to MoS<sub>x</sub> cannot be found in MoS<sub>x</sub>/UCN samples. This may be due to the amorphous structure of MoS<sub>x</sub>, and at the same time the broad diffraction peak of amorphous MoS<sub>x</sub> is too weak compared with the diffraction peak of the UCN crystal. The existence of MoS<sub>x</sub> in the MoS<sub>x</sub>/UCN composite will be confirmed further by our other tests.

The morphology and microstructure of UCN, MoS<sub>x</sub> and MoS<sub>x</sub>/UCN samples were investigated by TEM characterization, and the results are shown in Fig. 3. Fig. 3(a) shows the two-dimensional morphology of the synthesized MoS<sub>x</sub>. Fig. 3(b) presents the typical TEM image of MoS<sub>x</sub>/UCN, which has a two-dimensional morphology similar to that of pure g-C<sub>3</sub>N<sub>4</sub> nanosheets.<sup>36</sup> Fig. 3(c) is an HRTEM image of MoS<sub>x</sub>, a disordered structure in the plane is observed, which indicates that MoS<sub>x</sub> is amorphous. The lattice fringe of the MoS<sub>x</sub> nanosheet edge confirms its layered structure with an interlayer distance of 0.62 nm. Fig. 3(d) shows HRTEM images for MoS<sub>x</sub>/UCN (7 wt%). The layered structure of MoS<sub>x</sub> can also be found, which demonstrates that the layered MoS<sub>x</sub> co-catalysts are successfully loaded onto the surface of UCN. Fig. 3(e) is the HRTEM image of another area in MoS<sub>x</sub>/UCN (7 wt%). The lattice spacing in Fig. 3(e) is 0.27 nm, which corresponds to the (100) facets of 2H-MoS<sub>2</sub>. The lattice fringe of 2H-MoS<sub>2</sub> can be found because of the presence of partially crystalline MoS<sub>2</sub> in MoS<sub>x</sub>.<sup>29</sup> The co-existence of MoS<sub>2</sub> and MoS<sub>x</sub> is shown in Fig. S1.† The EDX pattern (Fig. 3(f)) of area I in Fig. 3(b) and elemental mapping (Fig. S2†) fully prove the combination of UCN and MoS<sub>x</sub> from another perspective. The BET specific surface area and pore volume of the samples are listed in Table S2.† The BET specific surface area of UCN and MoS<sub>x</sub>/UCN are 89.29 and 72.56 m<sup>2</sup> g<sup>-1</sup>, respectively. The pore volumes of UCN and MoS<sub>x</sub>/UCN are 0.31 and 0.18 m<sup>3</sup> g<sup>-1</sup>. After loading with MoS<sub>x</sub>, the specific surface area and pore volume of MoS<sub>x</sub>/UCN decreased, which may be caused by the MoS<sub>x</sub> covering the pores of UCN. The results indicate that a MoS<sub>x</sub>/UCN photocatalyst with a two-dimensional structure has been successfully prepared in this study.

X-ray photoelectron spectroscopy was carried out to check the chemical states of the elements in MoS<sub>x</sub>/UCN photocatalysts. Fig. 4(a) indicates the presence of S, Mo, C, N and O in MoS<sub>x</sub>/UCN samples. Fig. 4(b-e) show the high-resolution XPS spectra of C 1s, N 1s, Mo 3d and S 2p in the MoS<sub>x</sub>/UCN samples. The C 1s spectrum shown in Fig. 4(b) can be deconvoluted into three peaks at 284.6, 285.9 and 288.6 eV, which are ascribed to the sp<sup>2</sup>-bonded aromatic structure (N-C=N), graphitic carbon (C-C), and residual C-O, respectively.<sup>37,38</sup> As shown in Fig. 4(c), N 1s can be deconvoluted into three peaks at around 398.7 eV, 400.2 eV and 401.4 eV. The main peak at 398.7 eV can be assigned to sp<sup>2</sup> hybridized aromatic N bonded to carbon atoms (C=N-C).<sup>39</sup> In addition, the peaks at 400.2 eV and 401.4 eV are ascribed to the tertiary N bonded to carbon atoms in the form of N-(C)<sub>3</sub> and amino functional groups carrying

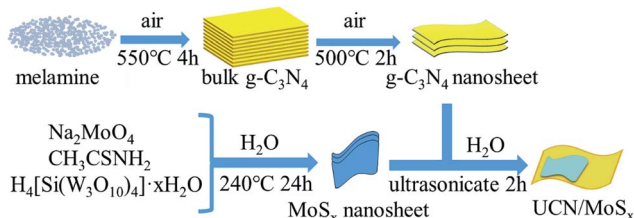


Fig. 1 Schematic diagram for the synthesis of MoS<sub>x</sub>/UCN composite.



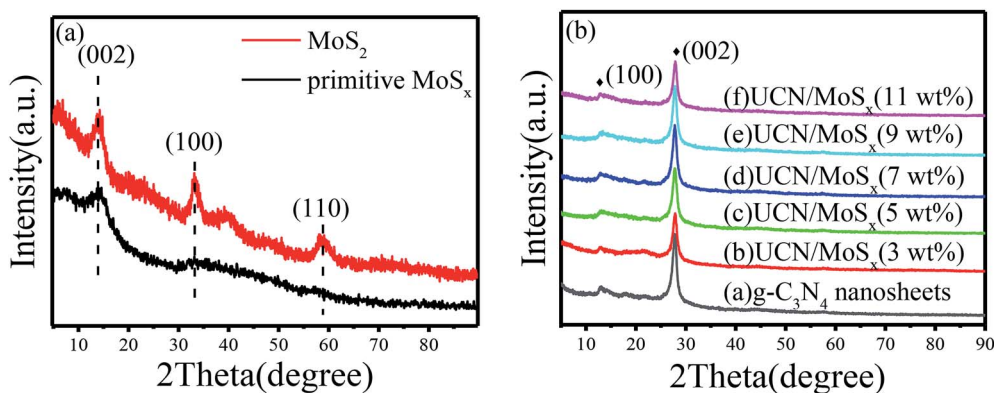


Fig. 2 XRD patterns of (a) primitive  $\text{MoS}_x$  and  $\text{MoS}_2$ , (b)  $\text{g-C}_3\text{N}_4$  nanosheets and  $\text{MoS}_x/\text{UCN}$  composite.

hydrogen ( $\text{C}-\text{N}-\text{H}$ ), respectively.<sup>40</sup> From Fig. 4(d), we can confirm that, except for two S 2s peaks at binding energies of 227.3 and 226.1 eV, other peaks can be readily assigned to the Mo 3d spectrum.<sup>41</sup> The peaks at 232.6 and 229.5 eV are attributed to Mo 3d<sub>3/2</sub> and Mo 3d<sub>5/2</sub>, which are binding energies for

Mo<sup>4+</sup> species in amorphous molybdenum sulfide.<sup>42</sup> The Mo 3d doublet at 229.8 and 233.3 eV may be attributed to Mo<sup>4+</sup> or Mo<sup>5+</sup> chemical state as in molybdenum oxysulfide  $\text{MoS}_x\text{O}_y$ , which can be surmised to be the presence of Mo=O defects in  $\text{MoS}_x/\text{UCN}$ .<sup>43,44</sup> Recently, Tran P. D. and colleagues found that Mo=O

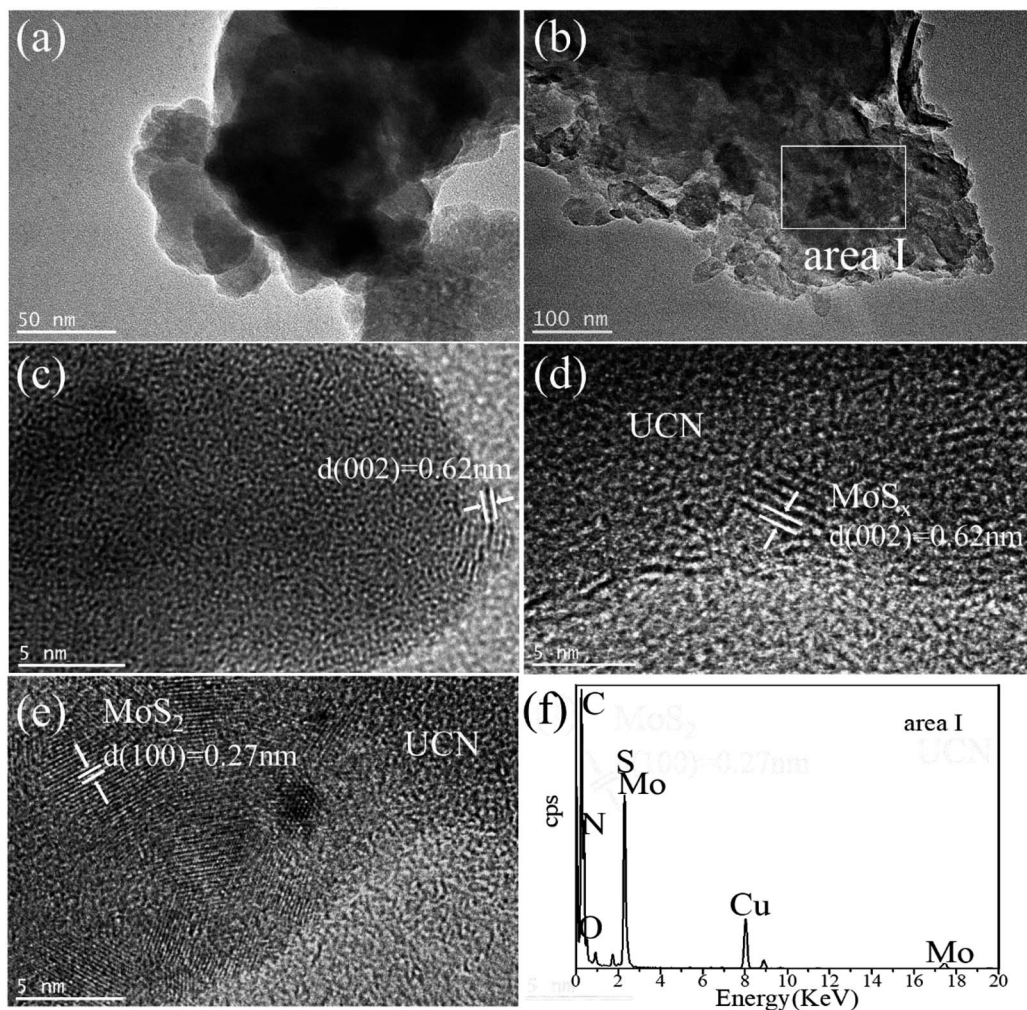


Fig. 3 TEM images of (a)  $\text{MoS}_x$  and (b) UCN; HRTEM images of (c)  $\text{MoS}_x$  and (d and e)  $\text{MoS}_x/\text{UCN}$ ; EDX pattern of (f) area I.

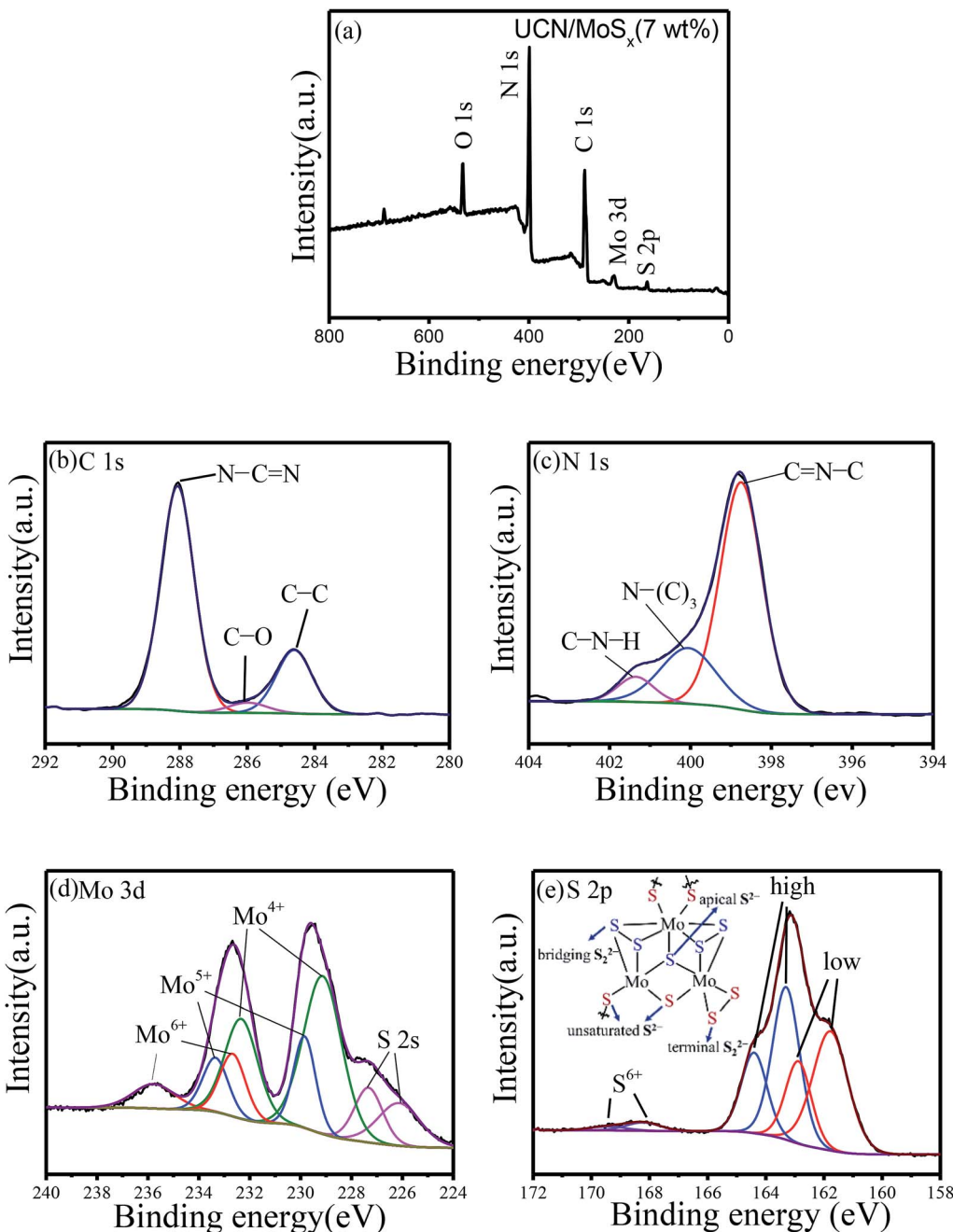


Fig. 4 Typical (a) XPS survey spectra and high-resolution XPS spectra of (b) C 1s, (c) N 1s, (d) Mo 3d and (e) S 2p.

defects will translate into Mo-bound hydride species which can act as the active species for  $H_2$ -evolution.<sup>45</sup> The doublet for Mo 3d at 233.1 and 236.1 eV suggests the presence of  $Mo^{6+}$ , indicating the formation of small amounts of surface oxide species.<sup>23</sup> The high-resolution XPS spectra of S 2p suggest the existence of both disulfide  $S_2^{2-}$  and monosulfide  $S^{2-}$ , as shown in Fig. 4(e).<sup>46,47</sup> And the higher binding energy signals (at 163.1 and 164.2 eV) are assigned to apical  $S_2^{2-}$  or bridging  $S_2^{2-}$ , while the lower higher binding energy signals (at 161.3 and 162.6 eV) are assigned to unsaturated  $S_2^{2-}$  or terminal  $S_2^{2-}$ .<sup>31,48</sup> The S atoms with high binding energy have better catalytic performance for the catalyst than those with low binding energy.<sup>49</sup> The

percentage of S atoms with high binding energy in  $MoS_x$  is about 50%, which is conducive to the  $MoS_x$  co-catalyst displaying a superior catalytic performance to crystalline  $MoS_2$ . The peaks at 168.2 and 169.4 eV could be attributed to  $S^{6+}$  or  $S^{4+}$  in surface oxide species. High-resolution XPS spectra of Mo 3d and S 2p in  $MoS_2$  are shown in Fig. S3,<sup>†</sup> which shows a marked difference from  $MoS_x$ . Furthermore, the atomic ratio of S/Mo was estimated as 2.7 according to XPS, which is higher than that of highly crystalline  $MoS_2$ .<sup>50</sup>

The UV-vis diffuse reflectance spectra of UCN and  $MoS_x$ /UCN are shown in Fig. 5(a). Pure UCN shows an absorption edge at 415 nm, which is consistent with previous studies.<sup>50,51</sup>

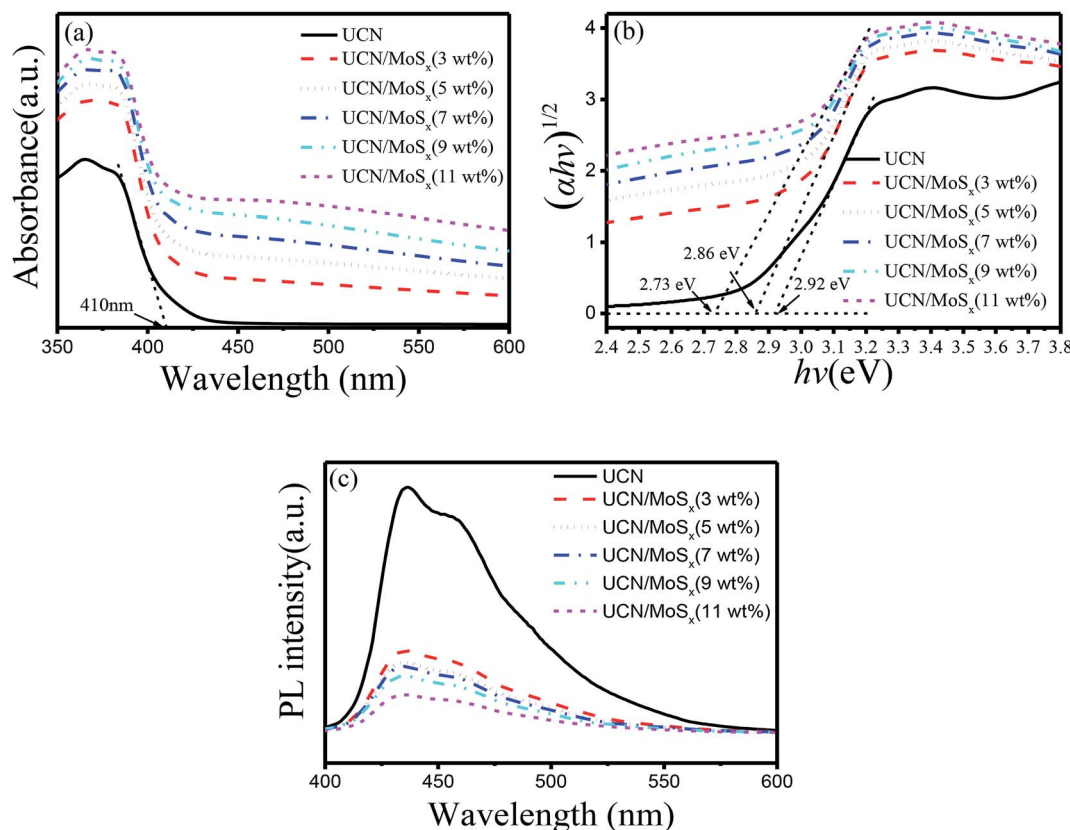


Fig. 5 Photoresponse properties of samples: (a) UV-vis diffuse reflectance spectra, (b) Tauc plots and  $E_g$  values and (c) photoluminescence spectra.

Compared with UCN, the  $\text{MoS}_x/\text{UCN}$  composite exhibits a red-shift of the absorption edge and obviously enhanced light absorption in the visible region. The magnitude of the red-shift and the enhancement in light absorption gradually increase with increasing  $\text{MoS}_x$  content. At the same time, the color of the prepared samples also changes from light yellow to dark gray. Fig. 5(b) shows that the  $E_g$  value of UCN is 2.92 eV and the  $E_g$  value of  $\text{MoS}_x/\text{UCN}$  (3–11 wt%) is 2.86–2.73 eV. In short,  $\text{MoS}_x$  expands the visible light-harvesting ability and narrows the  $E_g$  value of the UCN photocatalyst. This lets the photocatalyst absorb more photons, thereby enhancing its photocatalytic properties. In addition, as shown in Fig. 5(c), the photo-luminescence emission of UCN is remarkably quenched after  $\text{MoS}_x$  has been loaded onto it. And the intensity of the PL emission peaks for the  $\text{MoS}_x/\text{UCN}$  composite gradually decreases with an increase in  $\text{MoS}_x$  content, which means that  $\text{MoS}_x$  loading on the UCN surface can greatly suppress the rapid recombination of photogenerated electron–hole pairs in UCN. The results of UV-vis and PL measurements further prove that  $\text{MoS}_x$  has been successfully deposited onto the surface of UCN, and 2D  $\text{MoS}_x/\text{UCN}$  heterojunctions have been constructed.

### 3.2 Photocatalytic $\text{H}_2$ -evolution activity

The photocatalytic  $\text{H}_2$ -evolution performance of pure UCN,  $\text{MoS}_2/\text{UCN}$  (7 wt%) and UCN/ $\text{MoS}_x$  with different percentages

of  $\text{MoS}_x$  were evaluated under visible light irradiation ( $\lambda > 400$  nm) using triethanolamine as a sacrificial reagent. Fig. 6(a) shows the  $\text{H}_2$ -evolution rate by pure UCN and the  $\text{MoS}_x/\text{UCN}$  composite. The linearly increasing rate of  $\text{H}_2$ -evolution clearly shows that the  $\text{MoS}_x/\text{UCN}$  composite photocatalysts exhibit very good photostability within five hours. Further comparison of the average photocatalytic  $\text{H}_2$ -evolution rates of various photocatalysts is shown in Fig. 6(b). It can be seen that the  $\text{H}_2$ -evolution rate of pure UCN is only  $23 \mu\text{mol g}^{-1} \text{h}^{-1}$ , due to its fast recombination of electron–hole pairs. After 3–7 wt%  $\text{MoS}_x$  have combined with UCN, the average hydrogen-evolution rates of  $\text{MoS}_x/\text{UCN}$  increase to an optimal value of  $1586 \mu\text{mol g}^{-1} \text{h}^{-1}$ . With a further increase in  $\text{MoS}_x$  from 7 wt% to 11 wt%, the average  $\text{H}_2$ -evolution rate begins to decrease from  $1586 \mu\text{mol g}^{-1} \text{h}^{-1}$  to  $994 \mu\text{mol g}^{-1} \text{h}^{-1}$ . We also found that the photocatalytic activity of  $\text{MoS}_2/\text{UCN}$  is much lower than that of  $\text{MoS}_x/\text{UCN}$ , which indicates that as a co-catalyst  $\text{MoS}_x$  is much better than crystal  $\text{MoS}_2$ . It is obvious that the photocatalytic activity of the binary composite photocatalysts is much higher than that of the pure UCN photocatalyst. The most outstanding  $\text{H}_2$ -evolution rate of the  $\text{MoS}_x/\text{UCN}$  (7 wt%) photocatalyst is about 70 times that of pure UCN. In addition,  $\text{MoS}_x$  itself does not show such high photocatalytic activity for hydrogen evolution under visible light irradiation in the test, which confirms that  $\text{MoS}_x$  only plays the role of co-catalyst in  $\text{MoS}_x/\text{UCN}$ . In order to investigate the photocatalytic stability

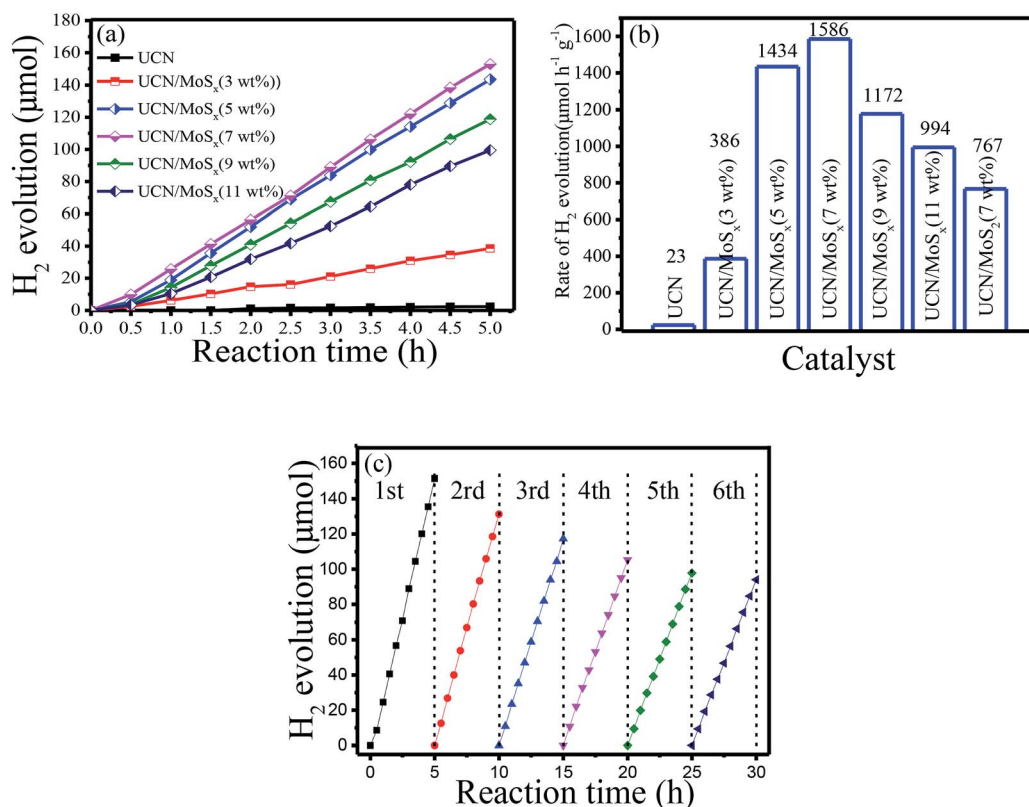


Fig. 6 Photocatalytic H<sub>2</sub>-evolution properties of samples: (a) the photocatalytic H<sub>2</sub>-evolution activities, (b) the photocatalytic H<sub>2</sub>-evolution rate and (c) cycle run tests for photocatalytic H<sub>2</sub>-evolution on MoS<sub>x</sub>/UCN (7 wt%).

of the MoS<sub>x</sub>/UCN composite, cycle running tests were conducted under visible light irradiation and are shown in Fig. 6(c). The activity of the photocatalyst decreases quickly with the first three cycle tests. This phenomenon could be induced by the degradation of MoS<sub>x</sub>. After the fourth cycle, the H<sub>2</sub>-evolution volume remains at about 62% of the H<sub>2</sub> volume produced with the first run test. From these results, deposition of MoS<sub>x</sub> on the surface of UCN plays a decisive role in enhancing the photocatalytic activity of H<sub>2</sub>-evolution. As mentioned, on the one hand, MoS<sub>x</sub> can improve the electron-hole separation efficiency as well as the visible light response of UCN; on the other hand, MoS<sub>x</sub> can provide a large number

of active sites for H<sub>2</sub>-evolution. However, excessive MoS<sub>x</sub> above 7 wt% may lead to a lower H<sub>2</sub>-evolution rate, which can be caused by the shielding effects of MoS<sub>x</sub> for both the surface active sites and the visible light response of UCN.<sup>52,53</sup> For comparison, the results of our research work and other reports are listed in Table S1.† The MoS<sub>x</sub>/UCN samples in our research work show much better photocatalytic activity for H<sub>2</sub>-evolution compared with most of the other research.

### 3.3 Photoelectrochemical measurements

To further confirm the elevated separation efficiency of photo-generated carriers and the transfer rate of charge carriers for

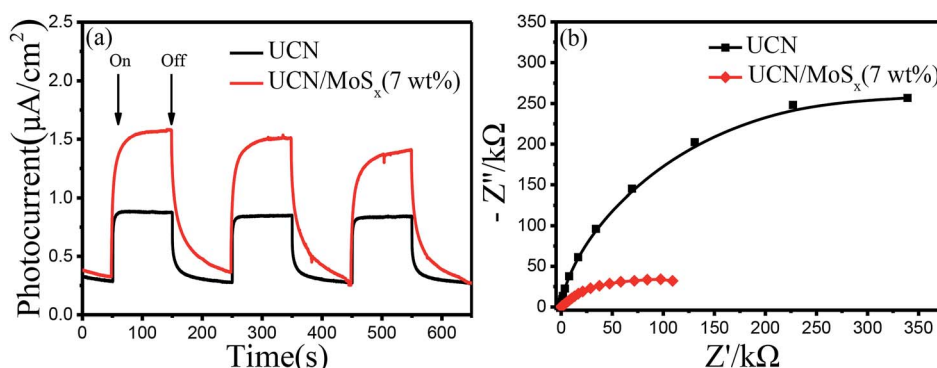


Fig. 7 (a) Photocurrent responses and (b) electrochemical impedance spectroscopy of samples.

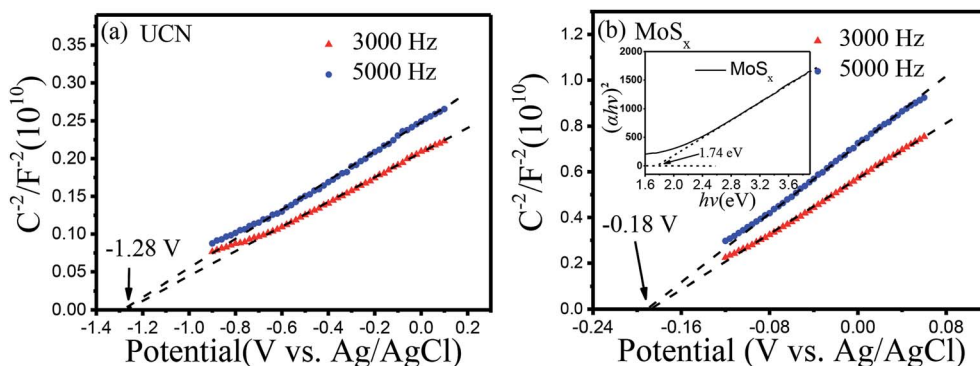


Fig. 8 Mott–Schottky plots of samples: (a) UCN, (b)  $\text{MoS}_x$ .

photocatalysts, the transient photocurrent response ( $I$ - $t$  curves) and the electrochemical impedance spectroscopy (EIS) of pure UCN and the  $\text{MoS}_x$ /UCN (7 wt%) composite photocatalysts performed by a typical three-electrode system are shown in Fig. 7. The photocurrent of the  $\text{MoS}_x$ /UCN (7 wt%) under visible light is almost twice that of UCN, as shown in Fig. 7(a). The higher photocurrent of  $\text{MoS}_x$ /UCN (7 wt%) can be ascribed to the introduction of  $\text{MoS}_x$ , which increases the separation of electron–hole pairs. As shown in Fig. 7(b), it is obvious that  $\text{MoS}_x$ /UCN (7 wt%) exhibits a smaller arc size compared to that of pure UCN, suggesting that the addition of  $\text{MoS}_x$  can accelerate the electron transfer through the intimate interfaces between UCN and  $\text{MoS}_x$ .

In order to study the energy band structure of the semiconductor photocatalysts, a Mott–Schottky study was carried out. From the Mott–Schottky plots (Fig. 8), the conduction band potential of UCN and  $\text{MoS}_x$  can be estimated.<sup>54</sup> The conduction bands (CBs) are determined to be  $-1.28\text{ V}$  and  $-0.18\text{ V}$  (vs.  $E_{\text{Ag}/\text{AgCl}}$ , pH = 7) for UCN and  $\text{MoS}_x$ , respectively. The potentials are converted to the NHE scale according to the equation:<sup>55,56</sup>

$$E_{\text{NHE}} = E_{\text{Ag}/\text{AgCl}} + E_{\text{Ag}/\text{AgCl}}^0 (0.198\text{ V})$$

The recalculated valence band (VB) potentials of UCN and  $\text{MoS}_x$  are  $-1.08$  and  $0.02\text{ V}$  (vs.  $E_{\text{NHE}}$ , pH = 7), respectively.

Following the equation  $E_{\text{VB}} = E_{\text{CB}} + E_g/e$ , the valence band potentials for UCN and  $\text{MoS}_x$  are  $1.84$  and  $1.76\text{ V}$  (vs. NHE, pH = 7). The conduction band potential for pure UCN ( $-1.08\text{ V}$  vs.  $E_{\text{NHE}}$ , pH = 7) is more negative than the  $\text{H}^+$  reduction potential ( $-0.410\text{ V}$  vs.  $E_{\text{NHE}}$  at pH = 7), which is enough to reduce  $\text{H}^+$  and produce  $\text{H}_2$ . The conduction band potential of pure  $\text{MoS}_x$  is more positive than the  $\text{H}^+$  reduction potential when the pH value equals 7, which results in an inertness of HER for  $\text{MoS}_x$  under visible irradiation. The result is consistent with the studies of previous reports.<sup>57</sup>

### 3.4 Photocatalytic mechanism

Based on the experimental results, a possible mechanism is proposed to explain the enhanced  $\text{H}_2$ -production activity of  $\text{MoS}_x$ /UCN. As shown in Fig. 9, the conduction band position for UCN is higher than that of  $\text{MoS}_x$ . Under visible light irradiation, UCN can capture the photons, and electrons in the valence band will transfer to the conduction band to form electron–hole pairs. After that, the electrons may move to the surface of UCN to reduce  $\text{H}^+$  and produce  $\text{H}_2$  by sufficient overpotential. But pure UCN shows poor  $\text{H}_2$ -evolution performance due to the lack of active species for  $\text{H}_2$  production. After deposition of  $\text{MoS}_x$ , the electrons excited on the surface of UCN can transfer to  $\text{MoS}_x$ , because the conduction band of  $\text{MoS}_x$  is more negative than that of UCN. First, the fast recombination of electron–hole

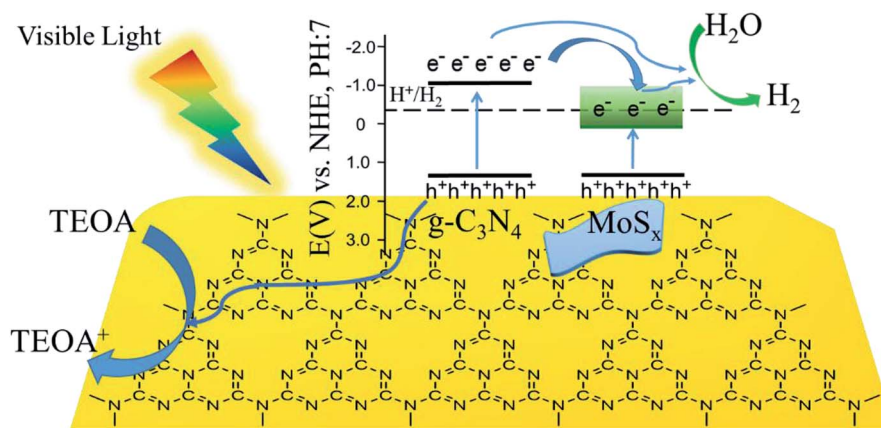


Fig. 9 Schematic illustration of the proposed principle of photocatalytic  $\text{H}_2$ -evolution by  $\text{MoS}_x$ /UCN under visible light irradiation.



pairs in UCN can be suppressed, and, second, the rapid consumption of electrons on the  $\text{MoS}_x$  surface may lead to the production of more  $\text{H}_2$ . Meanwhile, the holes in the VB of UCN are consumed by the triethanolamine sacrificial reagent. Furthermore, compared to  $\text{MoS}_2$ ,  $\text{MoS}_x$  has a larger number of unsaturated S-atoms and unsaturated Mo-atoms. Unsaturated S-atoms and unsaturated Mo-atoms can absorb  $\text{H}^+$  to form S–H and Mo–H bonds,<sup>45,49</sup> which can work as active species for  $\text{H}_2$  production, so  $\text{MoS}_x$  shows better co-catalytic performance than  $\text{MoS}_2$ .

## 4. Conclusion

In conclusion, a facile sonochemical approach was used to fabricate an  $\text{MoS}_x$ /UCN composite photocatalyst for superior photocatalytic  $\text{H}_2$  production. The results demonstrate that amorphous  $\text{MoS}_x$  loaded on UCN plays a co-catalyst role, the range of visible light absorption has been expanded, a large number of active species has been offered, and the separation and transportation of charge carriers have been promoted, leading to a tremendous improvement in the photocatalytic activity of UCN under visible light irradiation. For  $\text{MoS}_x$ /UCN, the optimal content of  $\text{MoS}_x$  is 7 wt%, in which the rate of  $\text{H}_2$ -evolution can reach a maximum value of  $1586 \mu\text{mol g}^{-1} \text{ h}^{-1}$ . The present work successfully provides a novel  $\text{g-C}_3\text{N}_4$  and amorphous  $\text{MoS}_x$  binary photocatalyst with excellent photocatalytic hydrogen-evolution performance.

## Conflicts of interest

There are no conflicts to declare.

## Acknowledgements

This work was financially supported by the National Natural Science Foundation of China (51770000), Natural Science Foundation of Anhui Province (1608085QE000), the Fundamental Research Funds for the Central Universities (JZ2017HGTB000), Guangxi Key Laboratory for Electrochemical Energy Materials, and the 111 Project “New Materials and Technology for Clean Energy” (B18018).

## References

- 1 L. M. Dai, D. W. Chang, J. B. Baek and W. Lu, *Small*, 2012, **8**, 1130–1166.
- 2 S. Wei, H. He, Y. Cheng, C. Yang, G. Zeng, L. Kang, H. Qian and C. Zhu, *Fuel*, 2017, **200**, 11–21.
- 3 E. Baran and B. Yazici, *Int. J. Hydrogen Energy*, 2016, **41**, 2498–2511.
- 4 K. Tedsee, T. Li, S. Jones, C. W. A. Chan, K. M. K. Yu, P. A. J. Bagot, E. A. Marquis, G. D. W. Smith and S. C. E. Tsang, *Nat. Nanotechnol.*, 2011, **6**, 302–307.
- 5 M. Z. Ge, J. S. Cai, J. Iocozzia, C. Y. Cao, J. Y. Huang, X. N. Zhang, J. L. Shen, S. C. Wang, S. N. Zhang, K. Q. Zhang, Y. K. Lai and Z. Q. Lin, *Int. J. Hydrogen Energy*, 2017, **42**, 8418–8449.
- 6 W. Zhang, Y. B. Wang, Z. Wang, Z. Y. Zhong and R. Xu, *Chem. Commun.*, 2010, **46**, 7631–7633.
- 7 T. Simon, N. Bouchonville, M. J. Berr, A. Vaneski, A. Adrovic, D. Volbers, R. Wyrwich, M. Doblinger, A. S. Susha, A. L. Rogach, F. Jackel, J. K. Stolarczyk and J. Feldmann, *Nat. Mater.*, 2014, **13**, 1013–1018.
- 8 Q. Xiang, J. Yu and M. Jaroniec, *Nanoscale*, 2011, **3**, 3670–3678.
- 9 S. C. Yan, Z. S. Li and Z. G. Zou, *Langmuir*, 2009, **25**, 10397–10401.
- 10 S. C. Yan, Z. S. Li and Z. G. Zou, *Langmuir*, 2010, **26**, 3894–3901.
- 11 X. Wang, K. Maeda, A. Thomas, K. Takanabe, G. Xin, J. M. Carlsson, K. Domen and M. Antonietti, *Nat. Mater.*, 2009, **8**, 76–80.
- 12 Y. W. Zhang, J. H. Liu, G. Wu and W. Chen, *Nanoscale*, 2012, **4**, 5300–5303.
- 13 B. Chai, T. Peng, J. Mao, K. Li and L. Zan, *Phys. Chem. Chem. Phys.*, 2012, **14**, 16745–16752.
- 14 Q. Han, B. Wang, J. Gao, Z. Cheng, Y. Zhao, Z. Zhang and L. Qu, *ACS Nano*, 2016, **10**, 2745–2751.
- 15 X. Wang, K. Maeda, X. Chen, K. Takanabe, K. Domen, Y. Hou, X. Fu and M. Antonietti, *J. Am. Chem. Soc.*, 2009, **131**, 1680.
- 16 J. Zhang, M. Zhang, C. Yang and X. Wang, *Adv. Mater.*, 2014, **26**, 4121–4126.
- 17 S. Hu, F. Li, Z. Fan, F. Wang, Y. Zhao and Z. Lv, *Dalton Trans.*, 2015, **44**, 1084–1092.
- 18 G. Liu, P. Niu, C. Sun, S. C. Smith, Z. Chen, G. Q. Lu and H.-M. Cheng, *J. Am. Chem. Soc.*, 2010, **132**, 11642–11648.
- 19 Z. Zhu, Z. Lu, D. Wang, X. Tang, Y. Yan, W. Shi, Y. Wang, N. Gao, X. Yao and H. Dong, *Appl. Catal., B*, 2016, **182**, 115–122.
- 20 O. Elbanna, M. Fujitsuka and T. Majima, *ACS Appl. Mater. Interfaces*, 2017, **9**, 34844–34854.
- 21 J. D. Benck, T. R. Hellstern, J. Kibsgaard, P. Chakthranont and T. F. Jaramillo, *ACS Catal.*, 2014, **4**, 3957–3971.
- 22 S. R. Kadam, D. J. Late, R. P. Panmand, M. V. Kulkarni, L. K. Nikam, S. W. Gosavi, C. J. Park and B. B. Kale, *J. Mater. Chem. A*, 2015, **3**, 21233–21243.
- 23 Y. Hou, A. B. Laursen, J. Zhang, G. Zhang, Y. Zhu, X. Wang, S. Dahl and I. Chorkendorff, *Angew. Chem., Int. Ed.*, 2013, **52**, 3621–3625.
- 24 L. Ge, C. Han, X. Xiao and L. Guo, *Int. J. Hydrogen Energy*, 2013, **38**, 6960–6969.
- 25 B. Han, S. Q. Liu, N. Zhang, Y. J. Xu and Z. R. Tang, *Appl. Catal., B*, 2017, **202**, 298–304.
- 26 M. Latorre-Sanchez, I. Esteve-Adell, A. Primo and H. Garcia, *Carbon*, 2015, **81**, 587–596.
- 27 Y. J. Yuan, Z.-J. Ye, H.-W. Lu, B. Hu, Y. H. Li, D.-Q. Chen, J.-S. Zhong, Z.-T. Yu and Z.-G. Zou, *ACS Catal.*, 2016, **6**, 532–541.
- 28 Q. Liu, Q. Fang, W. S. Chu, Y. Y. Wan, X. L. Li, W. Y. Xu, M. Habib, S. Tao, Y. Zhou, D. B. Liu, T. Xiang, A. Khalil, X. J. Wu, M. Chhowalla, P. M. Ajayan and L. Song, *Chem. Mater.*, 2017, **29**, 4738–4744.



29 S. C. Lee, J. D. Benck, C. Tsai, J. Park, A. L. Koh, F. Abild-Pedersen, T. F. Jaramillo and R. Sinclair, *ACS Nano*, 2016, **10**, 624–632.

30 H. Yu, P. Xiao, P. Wang and J. Yu, *Appl. Catal., B*, 2016, **193**, 217–225.

31 X. Hai, W. Zhou, K. Chang, H. Pang, H. Liu, L. Shi, F. Ichihara and J. Ye, *J. Mater. Chem. A*, 2017, **5**, 8591–8598.

32 P. Niu, L. Zhang, G. Liu and H.-M. Cheng, *Adv. Funct. Mater.*, 2012, **22**, 4763–4770.

33 Y. Hou, Z. Wen, S. Cui, X. Guo and J. Chen, *Adv. Mater.*, 2013, **25**, 6291–6297.

34 W. Zhou, Z. Yin, Y. Du, X. Huang, Z. Zeng, Z. Fan, H. Liu, J. Wang and H. Zhang, *Small*, 2013, **9**, 140–147.

35 H. Lin, X. Chen, H. Li, M. Yang and Y. Qi, *Mater. Lett.*, 2010, **64**, 1748–1750.

36 Q. Liu, T. Chen, Y. Guo, Z. Zhang and X. Fang, *Appl. Catal., B*, 2016, **193**, 248–258.

37 J. Mao, T. Peng, X. Zhang, K. Li, L. Ye and L. Zan, *Catal. Sci. Technol.*, 2013, **3**, 1253–1260.

38 Y. P. Liu, P. Chen, Y. Chen, H. D. Lu, J. X. Wang, Z. S. Yang, Z. H. Lu, M. Li and L. Fang, *RSC Adv.*, 2016, **6**, 10802–10809.

39 X. D. Zhang, X. Xie, H. Wang, J. J. Zhang, B. C. Pan and Y. Xie, *J. Am. Chem. Soc.*, 2013, **135**, 18–21.

40 X. Yuan, C. Zhou, Y. Jin, Q. Jing, Y. Yang, X. Shen, Q. Tang, Y. Mu and A.-K. Du, *J. Colloid Interface Sci.*, 2016, **468**, 211–219.

41 H. Vrubel and X. Hu, *ACS Catal.*, 2013, **3**, 2002–2011.

42 A. Y. Lu, X. Yang, C. C. Tseng, S. Min, S. H. Lin, C. L. Hsu, H. Li, H. Idriss, J.-L. Kuo, K.-W. Huang and L.-J. Li, *Small*, 2016, **12**, 5530–5537.

43 P. Kien-Cuong, D. S. McPhail, A. T. S. Wee and D. H. C. Chua, *RSC Adv.*, 2017, **7**, 6856–6864.

44 Y. Chen, P. D. Tran, P. Boix, Y. Ren, S. Y. Chiam, Z. Li, K. Fu, L. H. Wong and J. Barber, *ACS Nano*, 2015, **9**, 3829–3836.

45 P. D. Tran, T. V. Tran, M. Orio, S. Torelli, Q. D. Truong, K. Nayuki, Y. Sasaki, S. Y. Chiam, R. Yi, I. Honma, J. Barber and V. Artero, *Nat. Mater.*, 2016, **15**, 640.

46 D. Merki, S. Fierro, H. Vrubel and X. Hu, *Chem. Sci.*, 2011, **2**, 1262–1267.

47 L. Ye, D. Wang and S. Chen, *ACS Appl. Mater. Interfaces*, 2016, **8**, 5280–5289.

48 J. Kibsgaard, T. F. Jaramillo and F. Besenbacher, *Nat. Chem.*, 2014, **6**, 248–253.

49 L. R. L. Ting, Y. Deng, L. Ma, Y.-J. Zhang, A. A. Peterson and B. S. Yeo, *ACS Catal.*, 2016, **6**, 861–867.

50 K. K. Liu, W. J. Zhang, Y. H. Lee, Y. C. Lin, M. T. Chang, C. Y. Su, C. S. Chang, H. Li, Y. M. Shi, H. Zhang, C. S. Lai and L. J. Li, *Nano Lett.*, 2012, **12**, 1538–1544.

51 F. Dong, Y. Li, Z. Wang and W.-K. Ho, *Appl. Surf. Sci.*, 2015, **358**, 393–403.

52 Y. Min, G. He, Q. Xu and Y. Chen, *J. Mater. Chem. A*, 2014, **2**, 2578–2584.

53 K. Chang, Z. Mei, T. Wang, Q. Kang, S. Ouyang and J. Ye, *ACS Nano*, 2014, **8**, 7078–7087.

54 T. Giannakopoulou, I. Papailias, N. Todorova, N. Boukos, Y. Liu, J. Yu and C. Trapalis, *Chem. Eng. J.*, 2017, **310**, 571–580.

55 S. Hong, D. P. Kumar, D. A. Reddy, J. Choi and T. K. Kim, *Appl. Surf. Sci.*, 2017, **396**, 421–429.

56 M. Li, L. Zhang, X. Fan, M. Wu, Y. Du, M. Wang, Q. Kong, L. Zhang and J. Shi, *Appl. Catal., B*, 2016, **190**, 36–43.

57 Q. Xiang, B. Cheng and J. Yu, *Angew. Chem., Int. Ed.*, 2015, **54**, 11350–11366.

